HIGH-RESOLUTION FINITE VOLUME METHODS FOR DUSTY GAS JETS AND PLUMES[*]

MARICA PELANTI[†] AND RANDALL J. LEVEQUE[†]

Abstract. We consider a model for dusty gas flow that consists of the compressible Euler equations for the gas coupled to a similar (but pressureless) system of equations for the mass, momentum, and energy of the dust. These sets of equations are coupled via drag terms and heat transfer. A high-resolution wave-propagation algorithm is used to solve the equations numerically. The one-dimensional algorithm is shown to give agreement with a shock tube test problem in the literature. The two-dimensional algorithm has been applied to model explosive volcanic eruptions in which an axisymmetric jet of hot dusty gas is injected into the atmosphere and the expected behavior is observed at two different vent velocities. The methodology described here, with extensions to three dimensions and adaptive mesh refinement, is being used for more detailed studies of volcanic jet processes.

Key words. finite volume methods, high-resolution methods, volcanic flows, dusty gas, plumes, jets, shocks

AMS subject classifications. 65M06, 76T15

DOI. 10.1137/050635018

1. Introduction. We study compressible gas dynamics coupled with a suspended particulate phase having small volume fraction but possibly large density per unit volume relative to the gas. We refer to the particulate phase as "dust" (though in some contexts it could represent liquid droplets) and to the mixture as a "dusty gas." Dusty gas flows arise in many applications, from industrial processes to geophysical flows. One particular application, which was the original motivation for our work, is the study of volcanic ash plumes and pyroclastic flows. The numerical approach developed and tested here should be directly applicable in other contexts as well.

We ignore viscosity in the present work and use the compressible Euler equations to model the conservation of mass, momentum, and energy in the gas phase, using an ideal gas equation of state. The particulate phase is modeled by a similar system of equations for the conservation of mass, momentum, and energy of the dust. We ignore interparticle collisions and assume there is no pressure component in the momentum equations, using the so-called pressureless dust or sticky particle equations for this flow (see section 2). These two sets of conservation laws are coupled together through source terms that model drag and heat transfer between the phases.

In the absence of coupling terms, we would have two decoupled sets of hyperbolic conservation laws. The pressureless dust equations are nonstrictly hyperbolic (since the sound speed is zero in the absence of pressure) and have a degenerate structure in which delta shocks can arise, shocks at which delta function singularities form in this mathematical idealization. The source term coupling smooths out singularities in the solution. The speed of sound in the dusty gas is lower than the sound speed of the pure gas phase and can be substantially lower at high dust densities if there

---

[†]Department of Applied Mathematics, University of Washington, Box 352420, Seattle, WA 98195-2420 (pelanti@amath.washington.edu, rjl@amath.washington.edu).

is sufficient coupling, i.e., if the relaxation times of the momentum and heat transfer processes are sufficiently fast (see section 2.2). One effect of this is that dusty gas jets can be supersonic at relatively low velocities, and thus the shock wave structures typically seen in supersonic jets are often observed at lower velocities than might be expected. In particular, jets of ash in volcanic eruptions can exhibit such structures; see, e.g., [22].

The effect of gravity on both the gas and dust phases can also be included in the model when needed, as, for example, in the case of volcanic plumes, where gravity plays a substantial role. One question of particular interest in this context is whether an eruption column rises high into the atmosphere as a "Plinian column" and slowly disperses downwind, or whether the column collapses with the heavier dust phase flowing along the surface. This depends on the balance between the downward force of gravity and the upward momentum and buoyancy of the hot dense jet.

Applications to volcanic jets will be explored in more detail in a forthcoming paper [13] in which numerical results obtained with our approach will be compared with results from a similar model and different numerical method developed in the work of Neri, Esposti Ongaro, and co-workers [34, 36]. In the present paper we present the details of our numerical algorithm and several test problems.

The model is presented in more detail in section 2 and the numerical algorithm is developed in section 3. We use the wave-propagation algorithm as implemented in the CLAWPACK software [26]. This is a high-resolution finite volume algorithm for the hyperbolic conservation law portion of the equations, based on solving Riemann problems at each cell interface at every time step. We use the "f-wave formulation" [2, 29] of the algorithm in which the flux difference between neighboring cells is decomposed into waves that are then used to update the cell averages in each cell. This formulation is preferable for the pressureless dust portion of the hyperbolic system, where we use the algorithm developed in [30]. This formulation also allows us to incorporate the source term due to gravity in the gas dynamics portion of the hyperbolic system into the Riemann solver in such a way that hydrostatic balance in the atmosphere is well maintained in the absence of flow or dust (with the pressure gradient balancing the gravitational force on the gas). This is discussed in more detail in section 6, where gravity is introduced. The gravitational force in the dust equations and the source terms modeling interphase drag and heat transfer are all handled by a fractional step procedure, as described in section 5.

Our goal is to keep the physical model as simple as possible while still allowing simulation of some fundamental features of hot dilute dusty flows in the presence of gravity. In particular, we ignore viscosity within the gas phase and the effects of turbulence. In modeling the structure of dusty gas jets as considered here, this is a reasonable approximation.

Ultimately we hope that this approach will also be useful for modeling some aspects of volcanic eruptions in three dimensions over large domains to better understand hazards associated with active volcanos. For this it is desirable to have a simple model that is applicable on mapped grids that follow realistic terrain and to which adaptive mesh refinement can also be applied. The present model has been implemented on quadrilateral and hexahedral grids, and adaptive mesh refinement has been applied using both the AMRCLAW package included in CLAWPACK and the recently developed CHOMBO-CLAW package [5].

Extensive work has been done on dusty gas and related flows. The formulation that we adopt to describe the dynamics of this two-phase flow under the above assumptions follows especially the work of Harlow and Amsden [17], Sainsaulieu

[40, 42, 41], and Saito [43]. In particular, the physical and numerical model in [17] has been widely used in the field of geophysics to study the particle-laden flows ejected during volcanic eruptions, e.g., [46, 44, 10, 32, 36, 9]. A technique to obtain the macroscopic system of the presented model is the procedure described, e.g., in [19, 11], and applied by Sainsaulieu in [40], which consists in averaging the equations governing each single phase at the microscopic scale.

2. The equations for a dusty gas. We consider a two-phase flow composed of a gaseous carrier phase and a dispersed phase that can consist of either solid particles (dust) or liquid droplets, though we concentrate on the case of dust. In the following, the subscripts g and d will refer to the gas and the dust (or droplets), respectively. Each phase is modeled as a continuum described by macroscopic quantities, with the gas phase being compressible and the dispersed phase incompressible at a microscopic level (with microscopic density $\rho_d = $ constant within each particle or droplet). Moreover, we assume the carried phase is dilute; that is, its volume fraction $\vartheta_d \ll 1$.

2.1. One-dimensional equations. We first consider the one-dimensional equations in slightly more generality than we ultimately use computationally in order to discuss some of the physical and mathematical issues. In section 3 we discuss the numerical algorithms used in the context of the one-dimensional equations. In section 4 we present the relevant portion of these equations in three dimensions and discuss the multidimensional generalization of the numerical algorithm. Initially we ignore gravity and consider one-dimensional flow in the x-direction. In section 6 we discuss the manner in which gravity is incorporated into the algorithm.

In one space dimension the equations take the form

(1a)
$$\frac{\partial}{\partial t}\left(\vartheta_g \rho_g\right) + \frac{\partial}{\partial x}\left(\vartheta_g \rho_g u_g\right) = 0,$$

(1b)
$$\frac{\partial}{\partial t}\left(\vartheta_g \rho_g u_g\right) + \frac{\partial}{\partial x}\left(\vartheta_g \rho_g u_g^2 + \vartheta_g p_g\right) = p_g \frac{\partial \vartheta_g}{\partial x} - D(u_g - u_d),$$

(1c)
$$\frac{\partial}{\partial t}\left(\vartheta_g \rho_g e_g\right) + \frac{\partial}{\partial x}\left((\vartheta_g \rho_g e_g + \vartheta_g p_g)u_g\right)$$
$$= -p_g \frac{\partial}{\partial x}\left((1 - \vartheta_g)u_d\right) - D(u_g - u_d)u_d - \mathcal{Q}(T_g - T_d),$$

(1d)
$$\frac{\partial}{\partial t}\left(\vartheta_d \rho_d\right) + \frac{\partial}{\partial x}\left(\vartheta_d \rho_d u_d\right) = 0,$$

(1e)
$$\frac{\partial}{\partial t}\left(\vartheta_d \rho_d u_d\right) + \frac{\partial}{\partial x}\left(\vartheta_d \rho_d u_d^2 + \varphi\right) = -\vartheta_d \frac{\partial p_g}{\partial x} + D(u_g - u_d),$$

(1f)
$$\frac{\partial}{\partial t}\left(\vartheta_d \rho_d e_d\right) + \frac{\partial}{\partial x}\left((\vartheta_d \rho_d e_d + \varphi)u_d\right)$$
$$= -\vartheta_d u_d \frac{\partial p_g}{\partial x} + D(u_g - u_d)u_d + \mathcal{Q}(T_g - T_d).$$

Here ρ_g, ρ_d are the microscopic material densities, ϑ_g, ϑ_d the volume fractions, u_g, u_d the velocities along the x-axis, e_g, e_d the specific total energies, and T_g, T_d the temperatures. Moreover, p_g denotes the gas pressure and φ denotes a pressure correction

for the dispersed phase that will be set to zero below. Finally, D and $\mathcal{Q}$ express a drag and heat transfer function, respectively. To complete the description we need closure relations and specific expressions for D and $\mathcal{Q}$.

The specific total energies are related to the specific internal energies ε_g, ε_d through

$$(2) \qquad e_g = \varepsilon_g + \frac{1}{2}|u_g|^2 \quad \text{and} \quad e_d = \varepsilon_d + \frac{1}{2}|u_d|^2.$$

The gaseous phase is assumed to follow the ideal polytropic gas thermodynamic relations

$$(3a) \qquad p_g = (\gamma - 1)\rho_g \varepsilon_g, \quad \gamma = \text{constant},$$

$$(3b) \qquad \varepsilon_g = c_{vg} T_g, \quad c_{vg} = \text{constant}.$$

The pressure φ associated to the dispersed phase is small in comparison to the gas pressure p_g, and considering negligible interaction between particles (droplets), it can be assumed to be zero, as in [17, 43]. However, a nonzero φ plays an important role from a mathematical point of view, since the homogeneous equations of the dispersed phase lose strict hyperbolicity under the hypothesis $\varphi \equiv 0$. Following [41], here a nonzero φ is viewed as a pressure correction that allows one to maintain the strict hyperbolicity of the dispersed phase system. We will consider φ a function of the macroscopic density only:

$$(4) \qquad \varphi = \varphi(\beta), \quad \beta \equiv \vartheta_d \rho_d.$$

For instance, we can define φ based on the pressure law of the isothermal flow equations:

$$(5) \qquad \varphi(\beta) = a_d^2 \beta,$$

with a_d small. In [40, 41], where in particular the suspended phase is considered made of droplets, φ is expressed in the form

$$(6) \qquad \varphi = \varphi_0 \vartheta_d^\delta = \varphi_0 \left(\frac{\beta}{\rho_d}\right)^\delta,$$

where φ_0 is a constant proportional to the rest pressure of the gas flow on the droplets and $\delta = \frac{4}{3}$. Note that mathematically we recover (5) from (6) taking $\varphi_0 = \rho_d a_d^2$ and $\delta = 1$.

The specific internal energy of the dispersed phase is related to the temperature through a constant specific heat c_{vd}:

$$(7) \qquad \varepsilon_d = c_{vd} T_d, \quad c_{vd} = \text{constant}.$$

System (1) is closed by the equations (2), (3), (4), (7), together with the algebraic constraint $\vartheta_g + \vartheta_d = 1$, and definitions for the drag and heat transfer functions D and $\mathcal{Q}$.

The drag function D has the form (e.g., [31])

$$(8) \qquad D = \frac{3}{4} C_d \frac{\beta \rho}{\rho_d d}|u_g - u_d|,$$

where d is the dust particle diameter and C_{d} is the drag coefficient, which we express as in [10]:

$$
(9) \qquad C_{\mathrm{d}} = \begin{cases} \frac{24}{Re}\left(1 + 0.15 Re^{0.687}\right) & \text{if } Re < 1000, \\ 0.44 & \text{if } Re \geq 1000. \end{cases}
$$

Above $Re = \frac{\rho\, d |u_g - u_d|}{\mu}$ is the Reynolds number and μ the dynamic viscosity of the gas.

The heat transfer function is (see, e.g., [23])

$$
(10) \qquad \mathcal{Q} = \frac{Nu\, 6\kappa_g \beta}{\rho_d d^2},
$$

where $Nu = 2 + 0.65 Re^{1/2} Pr^{1/3}$ is the Nusselt number. Here $Pr = \frac{c_{pg}\mu}{\kappa_g}$ is the Prandtl number, κ_g the gas thermal conductivity, and c_{pg} the gas specific heat at constant pressure. In general, μ and κ_g will be assumed constant.

The momentum equations (1b), (1e) and the energy equations (1c), (1f) include nonconservative terms modeling exchange of momentum and energy related to the gas pressure gradient, namely $p_g \frac{\partial \vartheta_g}{\partial x}$, $p_g \frac{\partial}{\partial x}\left((1 - \vartheta_g) u_d\right)$, $\vartheta_d \frac{\partial p_g}{\partial x}$, and $\vartheta_d \frac{\partial p_g}{\partial x} u_d$. Under the hypothesis $\vartheta_d \ll 1$, these are small and give a weak coupling. They can be neglected, as in [43]. These nonconservative terms pose a mathematical difficulty when we wish to allow for discontinuous solutions of the two-phase system. An extensive mathematical analysis of the nonconservative system (1) without drag and heat transfer terms has been performed in [42, 41] by Sainsaulieu, who gives a definition of shock wave solutions for the two-phase nonconservative system and derives explicit approximate jump conditions for these discontinuous solutions, showing that they are perturbations of order $\varepsilon = \frac{1}{\rho_d} \ll 1$ of the decoupled jump conditions of the homogeneous system. Other work on nonconservative terms in nonlinear problems can be found, for example, in [1, 4, 8, 25].

In this work we drop these nonconservative terms, so that only drag and heat conduction source terms appear on the right-hand side of equations (1). We can then simplify the notation by introducing

$$
(11) \qquad \rho = \vartheta_g \rho_g, \quad p = \vartheta_g p_g, \quad E = \vartheta_g \rho_g e_g, \quad \beta = \vartheta_d \rho_d, \quad \Omega = \vartheta_d \rho_d e_d.
$$

The reduced equations can then be written as

$$
(12) \qquad q_t + f(q)_x = \psi(q),
$$

where q is the solution vector, which we partition into q_g, containing the mass, momentum, and energy of the gas, and q_d, containing these quantities for the dust. Then (12) is partitioned as

$$
(13) \qquad \frac{\partial}{\partial t}\begin{bmatrix} q_g \\ q_d \end{bmatrix} + \frac{\partial}{\partial x}\begin{bmatrix} f_g(q_g) \\ f_d(q_d) \end{bmatrix} = \begin{bmatrix} \psi_g(q) \\ \psi_d(q) \end{bmatrix},
$$

with

(14a)

$$
q_g = \begin{bmatrix} \rho \\ \rho u_g \\ E \end{bmatrix}, \quad f_g(q_g) = \begin{bmatrix} \rho u_g \\ \rho u_g^2 + p \\ (E + p) u_g \end{bmatrix}, \quad \psi_g = \begin{bmatrix} 0 \\ -D(u_g - u_d) \\ -D(u_g - u_d) u_d - \mathcal{Q}(T_g - T_d) \end{bmatrix},
$$

(14b)

$$q_d = \begin{bmatrix} \beta \\ \beta u_d \\ \Omega \end{bmatrix}, \quad f_d(q_d) = \begin{bmatrix} \beta u_d \\ \beta u_d^2 + \varphi \\ (\Omega + \varphi)u_g \end{bmatrix}, \quad \psi_d = \begin{bmatrix} 0 \\ D(u_g - u_d) \\ D(u_g - u_d)u_d + \mathcal{Q}(T_g - T_d) \end{bmatrix}.$$

Numerically we solve system (13) using a fractional step procedure in which we alternate between a time step on the homogeneous hyperbolic system $q_t + f(q)_x = 0$ and a time step on the source terms, the system of ODEs $q_t = \psi(q)$ in each grid cell. (The source term for gravity in the gas will be treated differently in section 6.)

Notice that q_g and q_d are coupled only through the source terms and so the hyperbolic part decouples into two smaller systems for the gas and dust separately. For the gas phase,

$$(15) \qquad \frac{\partial q_g}{\partial t} + \frac{\partial f_g(q_g)}{\partial x} = 0,$$

we have the standard Euler equations for gas dynamics for an ideal gas. This system has three distinct characteristic speeds u_g and $u_g \pm c_g$ given by the eigenvalues of the Jacobian matrix $f_g'(q_g)$, where c_g is the sound speed of the gas, and $c_g = \sqrt{\gamma p_g / \rho}$ for an ideal gas.

The equations for the dust phase are similar:

$$(16) \qquad \frac{\partial q_d}{\partial t} + \frac{\partial f_d(q_d)}{\partial x} = 0.$$

If we assume that the pressure correction φ depends only on β (e.g., (5)), then the energy equation simply models advection of energy at velocity u_d. This equation is coupled to the rest of the system, however, when the source terms are added due to energy transfer between the phases.

Dropping the energy equation from the hyperbolic system for the dust, we obtain the reduced system

$$(17) \qquad \frac{\partial}{\partial t}\begin{bmatrix} \beta \\ \beta u_d \end{bmatrix} + \frac{\partial}{\partial x}\begin{bmatrix} \beta u_d \\ \beta u_d^2 + \varphi \end{bmatrix} = \begin{bmatrix} 0 \\ 0 \end{bmatrix}.$$

The Jacobian matrix for this sytem has eigenvalues $u_d \pm c_d$, where $c_d = \sqrt{\varphi'(\beta)}$. For example, if we use the isothermal relation (5), $\varphi(\beta) = a_d^2 \beta$, then $c_d = a_d$. If we ignore interparticle collisions, then we want to consider the "pressureless" limit $a_d \to 0$, in which case the system (17) becomes nonstrictly hyperbolic with both eigenvalues equal to u_d, and the system (16) has all three eigenvalues equal to u_d. The Jacobian matrix lacks a complete set of eigenvectors in this case, and weak solutions to the equations can contain delta shocks—shock waves at which a delta function singularity of accumulated dust also arises [30].

The term "pressureless" is something of a misnomer when the limiting process described above is really intended, as we are considering the limit where interparticle collision effects play a role, but only when the density becomes very large. When the particulate phase is sufficiently dilute, the details of this interaction are unimportant and we can set $a_d = 0$. The drag coupling of these equations to the gas dynamics equations might be expected to yield a regularization effect preventing the formation of delta function singularities in the coupled system. We do not know of any theoretical work in this direction and believe that it would be an interesting topic to pursue.

Numerically we do not observe delta shocks in the coupled system, although numerical viscosity is also playing a role, and at any rate exact singularities could not arise in the numerical solution. More importantly, in practice the dust densities do not grow to levels that cause any difficulties near shocks.

2.2. The mixture speed of sound. Gas flows carrying a particulate phase may exhibit a sound speed that is much lower than the sound speed of the pure gas. Here we informally derive an expression for the speed of sound of the mixture of gas and particles, based on the model (1) with $\varphi \equiv 0$, under the assumption that momentum and energy exchange between the gas and dust occurs rapidly enough so that they are in mechanical and thermal equilibrium (*homogeneous flow* hypothesis). For example, this is often approximately satisfied in vast regions of the physical domain where volcanic processes occur. Note that we will not assume in general equilibrium between the two phases in our numerical method, but the expression of the mixture sound speed derived in this special case can be useful to estimate a posteriori the flow regime (subsonic/supersonic). Moreover we employ this expression in [38] to show that solving the coupled system handling the source terms by a fractional step approach is successful even in this equilibrium limit.

We consider the propagation of small-amplitude pressure waves (acoustic waves) against a steady background with constant velocities $u_{g0} = u_{d0} = 0$, constant densities $\rho_0 = \vartheta_{g0}\rho_{g0}$, $\beta_0 = \vartheta_{d0}\rho_d = (1 - \vartheta_{g0})\rho_d$ (recall that $\rho_d = $ const.), and constant gas pressure. We also assume that $c_{vd}\beta_0 \gg c_{vg}\rho_0$ so that the dust contains much more thermal energy than the gas. Since we are assuming the temperature equilibrates rapidly between the gas and dust and we are considering small perturbations about a constant state, it is then reasonable to assume that the dust acts as a heat reservoir that keeps the gas at a constant temperature as the acoustic wave propagates. We can then drop the corresponding source term and simply consider isothermal behavior. The effective equation of state is then

$$(18) \qquad p_g = a_g^2 \rho_g, \quad a_g^2 = R\bar{T}_g,$$

where a_g represents the isothermal sound speed of the pure gaseous phase and $\bar{T}_g$ denotes the constant temperature of the two-phase mixture. Under the above assumption of isothermal flow, and using (18), equations (1) give the reduced system

$$(19a) \qquad \frac{\partial}{\partial t}\left(\vartheta_g\rho_g\right) + \frac{\partial}{\partial x}\left(\vartheta_g\rho_g u_g\right) = 0,$$

$$(19b) \qquad \frac{\partial}{\partial t}\left(\vartheta_g\rho_g u_g\right) + \frac{\partial}{\partial x}\left(\vartheta_g\rho_g u_g^2\right) + a_g^2\vartheta_g\frac{\partial \rho_g}{\partial x} = -D(u_g - u_d),$$

$$(19c) \qquad \frac{\partial}{\partial t}\left((1 - \vartheta_g)\rho_d\right) + \frac{\partial}{\partial x}\left((1 - \vartheta_g)\rho_d u_d\right) = 0,$$

$$(19d) \qquad \frac{\partial}{\partial t}\left((1 - \vartheta_g)\rho_d u_d\right) + \frac{\partial}{\partial x}\left((1 - \vartheta_g)\rho_d u_d^2\right) + a_g^2(1 - \vartheta_g)\frac{\partial \rho_g}{\partial x} + D(u_g - u_d),$$

where we have also used the algebraic constraint $\vartheta_g + \vartheta_d = 1$. Considering small perturbations with respect to background variables, we write

$$(20) \qquad \rho_g = \rho_{g0} + \tilde{\rho}_g \qquad \text{and} \qquad \vartheta_g = \vartheta_{g0} + \tilde{\vartheta}_g.$$

Linearizing (19), and dividing the resulting continuity equations of the two phases by the corresponding background microscopic densities, we obtain

$$(21a) \qquad \frac{\vartheta_{g0}}{\rho_{g0}}\frac{\partial \tilde{\rho}_g}{\partial t} + \frac{\partial \tilde{\vartheta}_g}{\partial t} + \vartheta_{g0}\frac{\partial u_g}{\partial x} = 0,$$

$$(21b) \qquad \vartheta_{g0}\rho_{g0}\frac{\partial u_g}{\partial t} + a_g^2 \vartheta_{g0}\frac{\partial \tilde{\rho}_g}{\partial x} = -D(u_g - u_d),$$

$$(21c) \qquad -\frac{\partial \tilde{\vartheta}_g}{\partial t} + (1-\vartheta_{g0})\frac{\partial u_d}{\partial x} = 0,$$

$$(21d) \qquad (1-\vartheta_{g0})\rho_d\frac{\partial u_d}{\partial t} + a_g^2(1-\vartheta_{g0})\frac{\partial \tilde{\rho}_g}{\partial x} = D(u_g - u_d).$$

Adding now (21b) and (21d) eliminates the drag source term, and if we assume that this acts sufficiently fast that velocity perturbations satisfy $u_g = u_d \equiv u$, then the resulting equation along with the sum of (21a) and (21c) gives a reduced system of two equations for $\tilde{\rho}_g$ and u:

$$(22a) \qquad \frac{\vartheta_{g0}}{\rho_{g0}}\frac{\partial \tilde{\rho}_g}{\partial t} + \frac{\partial u}{\partial x} = 0,$$

$$(22b) \qquad (\vartheta_{g0}\rho_{g0} + (1-\vartheta_{g0})\rho_d)\frac{\partial u}{\partial t} + a_g^2\frac{\partial \tilde{\rho}_g}{\partial x} = 0.$$

This system has wave speeds $\pm c_{\mathrm{m}}$, where

$$(23) \qquad c_{\mathrm{m}} = a_g\sqrt{\frac{\rho_{g0}}{\vartheta_{g0}(\vartheta_{g0}\rho_{g0} + \vartheta_{d0}\rho_d)}}$$

is the mixture sound speed in the considered case of equilibrium flow. This expression can be derived more generally for the case in which the suspended phase is also compressible and governed by a nonzero pressure law, see, for example, [45, 11].

Under the assumption of a dilute dust phase, we can approximate $\vartheta_{g0} \approx 1$, and hence $\rho_{g0} \approx \rho_0$. Therefore, $c_{\mathrm{m}} \approx a_g\sqrt{\frac{\rho_0}{\rho_0+\beta_0}}$. This expression can also be obtained directly with a procedure analogous to that described above by neglecting in (1) the terms modeling momentum exchange due to the gas pressure gradient, which is again valid if $\vartheta_{g0} \approx 1$. This in particular suggests that neglecting pressure gradient terms in the hypothesis $\vartheta_d \ll 1$ still allows us to correctly model the propagation of acoustic waves.

Note that $c_{\mathrm{m}} < a_g < c_g = (\gamma R \bar{T}_g)^{1/2}$, where c_g is the isentropic pure gas sound speed (at same T_g) and, moreover, c_{m} can be significantly lower than a_g and c_g if β_0 is large compared to ρ_0.

It is interesting that this mixture sound speed arises only from the source terms coupling the gas and dust equations and can be significantly lower than the wave speeds given by the hyperbolic part of the system of equations. Numerical results presented in [38] show that using a fractional step approach in which the source terms are decoupled from the hyperbolic system, as described below, does give the correct behavior of the coupled system and the correct sound speed.

3. The numerical algorithm for the hyperbolic portion. To solve the homogeneous hyperbolic portion of the system (1) we use the wave-propagation algorithm described in [27, 29]. This is a Godunov-type finite volume method in which we first solve the Riemann problem at each interface between grid cells, i.e., the conservation law with piecewise constant initial data given by the current cell averages Q_{i-1}^n and Q_i^n at time t_n. The waves arising from this Riemann solution are used to update the cell average on either side. These waves are also used to define second-order correction terms based on Taylor series expansion. Near discontinuities such as shocks, however, these corrections do not improve the accuracy but instead lead to nonphysical oscillations in the numerical approximation. Hence limiters must be applied to the waves before using them in the correction terms in order to avoid oscillations and obtain high-resolution results. We use the "f-wave" formulation of these methods discussed in [2, 29]. With this approach the Riemann solution is represented by a decomposition of the flux difference $f(Q_i) - f(Q_{i-1})$ as a linear combination of eigenvectors of an approximate Jacobian matrix. Both the first-order Godunov updates and the second-order correction terms can be defined in terms of these f-waves, and the limiters are now applied to these f-waves before computing the correction terms. This formulation of the algorithm for the gas phase will be advantageous when we add gravity in section 6. For the dust phase it helps to simplify the treatment of the nonstrictly hyperbolic Riemann solution.

Recall that the hyperbolic equations decouple into separate systems (15) for the gas phase and (16) for the dust phase. To approximately solve the Riemann problem in the gas phase between states Q_g^{L} and Q_g^{R} in adjacent grid cells, we use the Roe linearization [29, 39] to define eigenvectors r^1, r^2, r^3 based on Roe averages of the solution quantities. We decompose

$$(24) \qquad f(Q_g^{\mathrm{R}}) - f(Q_g^{\mathrm{L}}) = \sum_{p=1}^{3} \mathcal{Z}_g^p,$$

where each f-wave $\mathcal{Z}_g^p$ is a scalar multiple of r^p.

For the dust phase we use the algorithm presented in [30]. For the pressureless dust equations the solution to the Riemann problem consists of either a single delta shock if $u_d^{\mathrm{L}} > u_d^{\mathrm{R}}$ or a pair of waves with a vacuum between them if $u_d^{\mathrm{L}} < u_d^{\mathrm{R}}$. With the f-wave formulation we generally use only a single wave in either case with magnitude $\mathcal{Z}_d = f(Q_d^{\mathrm{R}}) - f(Q_d^{\mathrm{L}})$ and speed

$$(25) \qquad \hat{u}_d = \frac{\sqrt{\beta^{\mathrm{L}}}\, u_d^{\mathrm{L}} + \sqrt{\beta^{\mathrm{R}}}\, u_d^{\mathrm{R}}}{\sqrt{\beta^{\mathrm{L}}} + \sqrt{\beta^{\mathrm{R}}}}.$$

This is the usual Roe average for the dust velocity, based on the dust density, and it can also be shown to be the correct delta-shock propagation speed in the pressureless equations [30]. The only time we use two waves is if $u_d^{\mathrm{L}} < 0 < u_d^{\mathrm{R}}$, in which case they are spreading out with a vacuum state at the interface. Then we take

$$(26) \qquad \begin{aligned} \mathcal{Z}_d^1 &= -f_d(Q_d^{\mathrm{L}}), & s^1 &= u_d^{\mathrm{L}}, \\ \mathcal{Z}_d^2 &= f_d(Q_d^{\mathrm{R}}), & s^2 &= u_d^{\mathrm{R}}, \end{aligned}$$

as the waves and speeds. For more details, see [30].

ϑ_g, ϑ_d = volume fractions, $\vartheta_g + \vartheta_d = 1$, $\vartheta_d \ll 1$;
ρ_g, ρ_d = material microscopic mass densities (ρ_d = constant);
$\rho = \vartheta_g \rho_g$ = gas macroscopic density;
$\beta = \vartheta_d \rho_d$ = dust macroscopic density (concentration);
p_g = gas pressure, $p = \vartheta_g p_g$;
$\mathcal{V}_g = (u_g, v_g, w_g)^{\mathrm{T}}$, $\mathcal{V}_d = (u_d, v_d, w_d)^{\mathrm{T}}$ = vectorial velocities;
$\varepsilon_g, \varepsilon_d$ = specific internal energies;
$e_g = \varepsilon_g + \frac{1}{2}|\mathcal{V}_g|^2$, $e_d = \varepsilon_d + \frac{1}{2}|\mathcal{V}_d|^2$ = specific total energies;
$E = \vartheta_g \rho_g e_g$, $\Omega = \vartheta_d \rho_d e_d$ = total energies per unit volume;
T_g, T_d = temperatures;
R = gas constant;
$\gamma = c_{pg}/c_{vg}$ = ratio of specific heats for gas;
c_{vd} = dust specific heat;
μ = gas dynamic viscosity;
κ_g = gas thermal conductivity;
$\mathfrak{g} = (0, 0, -g)^{\mathrm{T}}$ = gravity acceleration (z-direction);
D = drag function;
d = dust particle diameter;
C_{d} = drag coefficient;
$\mathcal{Q}$ = heat transfer function;
Re = Reynolds number;
Nu = Nusselt number;
Pr = Prandtl number.

4. The multidimensional equations and algorithm. The multidmensional equations we use have the form

$$\text{(27a)} \qquad \frac{\partial \rho}{\partial t} + \nabla \cdot (\rho \mathcal{V}_g) = 0,$$

$$\text{(27b)} \qquad \frac{\partial}{\partial t}(\rho \mathcal{V}_g) + \nabla \cdot (\rho \mathcal{V}_g \otimes \mathcal{V}_g + pI) = -D(\mathcal{V}_g - \mathcal{V}_d),$$

$$\text{(27c)} \qquad \frac{\partial E}{\partial t} + \nabla \cdot ((E + p)\mathcal{V}_g) = -D(\mathcal{V}_g - \mathcal{V}_d) \cdot \mathcal{V}_d - \mathcal{Q}(T_g - T_d),$$

$$\text{(27d)} \qquad \frac{\partial \beta}{\partial t} + \nabla \cdot (\beta \mathcal{V}_d) = 0,$$

$$\text{(27e)} \qquad \frac{\partial}{\partial t}(\beta \mathcal{V}_d) + \nabla \cdot (\beta \mathcal{V}_d \otimes \mathcal{V}_d) = D(\mathcal{V}_g - \mathcal{V}_d),$$

$$\text{(27f)} \qquad \frac{\partial \Omega}{\partial t} + \nabla \cdot (\Omega \mathcal{V}_d) = D(\mathcal{V}_g - \mathcal{V}_d) \cdot \mathcal{V}_d + \mathcal{Q}(T_g - T_d).$$

Here $\mathcal{V}_g = (u_g, v_g, w_g)^{\mathrm{T}}$ and $\mathcal{V}_d = (u_d, v_d, w_d)^{\mathrm{T}}$ are the velocity vectors (in the three-dimensional case). The closure relations are the same as those presented in section 2, and the drag and heat transfer terms are also unchanged except that now

$$\text{(28)} \qquad D = \frac{3}{4}C_{\mathrm{d}}\frac{\beta \rho}{\rho_d d}|\mathcal{V}_g - \mathcal{V}_d|$$

depends on the Euclidean norm of the velocity difference, as does the Reynolds number $Re = (\rho \, d|\mathcal{V}_g - \mathcal{V}_d|)/\mu$. See Table 1 for a summary of the nomenclature used.

The finite volume method is extended to multidimensions using the wave-propagation approach described in [24, 27, 29] and implemented in CLAWPACK. We assume

the grid is logically rectangular, but a grid mapping can be incorporated so that a general quadrilateral (in two dimensions) or hexahedral (in three dimensions) grid is used. The two-dimensional case is discussed in detail in [29].

In each time step, one-dimensional Riemann problems are solved normal to each cell interface and the resulting waves are used to update the cell averages on either side. For the dusty gas equations, the one-dimensional Riemann problem in an arbitrary direction takes the same form as the Riemann problem in the x-direction discussed in section 3, using the normal components of the gas and dust velocities in each grid cell to define the data. Jumps in transverse velocities advect with the flow, at the velocity of the contact discontinuity in the gas equations or of the delta shock in the dust phase. The waves resulting from these normal Riemann solutions are also used in second-order correction terms, just as in one dimension after suitable limiters have been applied to avoid nonphysical oscillations.

A "transverse Riemann solver" is also incorporated that takes the information propagating into each grid cell and splits this into eigenvectors of the flux Jacobian matrix (evaluated in the cell) in the direction orthogonal to each of the adjacent cell faces (for a nonorthogonal mapped grid this must be done separately for each adjacent face). Use of these transverse Riemann solvers increases the accuracy of the multidimensional method by modeling cross-derivative terms needed in the Taylor series expansion, and also improves stability so that a Courant number close to 1 can typically be used (see [24] for a detailed discussion of accuracy and stability issues in three dimensions).

5. Source terms for drag and heat transfer. We also use a fractional step approach in applying the source terms for drag and heat transfer, first solving the ODEs arising from the drag terms over a time step Δt and then solving the ODEs for heat transfer. For the drag terms we have the system of ODEs

$$(29a) \qquad \frac{\partial \rho}{\partial t} = 0,$$

$$(29b) \qquad \frac{\partial}{\partial t}(\rho \mathcal{V}_g) = -A|\mathcal{V}_g - \mathcal{V}_d|(\mathcal{V}_g - \mathcal{V}_d),$$

$$(29c) \qquad \frac{\partial E}{\partial t} = -A|\mathcal{V}_g - \mathcal{V}_d|(\mathcal{V}_g - \mathcal{V}_d) \cdot \mathcal{V}_d,$$

$$(29d) \qquad \frac{\partial \beta}{\partial t} = 0,$$

$$(29e) \qquad \frac{\partial}{\partial t}(\beta \mathcal{V}_d) = A|\mathcal{V}_g - \mathcal{V}_d|(\mathcal{V}_g - \mathcal{V}_d),$$

$$(29f) \qquad \frac{\partial \Omega}{\partial t} = A|\mathcal{V}_g - \mathcal{V}_d|(\mathcal{V}_g - \mathcal{V}_d) \cdot \mathcal{V}_d,$$

with initial data ρ^0, $(\rho \mathcal{V}_g)^0$, E^0, β^0, $(\beta \mathcal{V}_d)^0$, Ω^0 at the beginning of the time step that come from the hyperbolic solver.

The densities ρ and β are constant in this step. We also assume that the Reynolds number is constant in time, so that the drag coefficient is equal to its initial value, $C_{\mathrm{d}} = C_{\mathrm{d}}^0$. Then A is constant in time and equal to

$$(30) \qquad\qquad A^0 = \frac{3}{4} C_{\mathrm{d}}^0 \frac{\beta^0 \rho^0}{\rho_d d}.$$

Then we can write (29b), (29e) for the momentum of the two phases as

$$\text{(31a)} \qquad \frac{\partial \rho^0 \mathcal{V}_g}{\partial t} = -A^0 |\mathcal{V}_g - \mathcal{V}_d|(\mathcal{V}_g - \mathcal{V}_d),$$

$$\text{(31b)} \qquad \frac{\partial \beta^0 \mathcal{V}_d}{\partial t} = A^0 |\mathcal{V}_g - \mathcal{V}_d|(\mathcal{V}_g - \mathcal{V}_d).$$

These equations can be solved exactly to obtain

$$\text{(32a)} \qquad (\rho \mathcal{V}_g)(\Delta t) = (\rho \mathcal{V}_g)^0 + \frac{\mathcal{V}_g^0 - \mathcal{V}_d^0}{\xi_D^0} \left[\frac{1}{A^0 \xi_D^0 |\mathcal{V}_g^0 - \mathcal{V}_d^0| \Delta t + 1} - 1 \right],$$

$$\text{(32b)} \qquad (\beta \mathcal{V}_d)(\Delta t) = (\beta \mathcal{V}_d)^0 - \frac{\mathcal{V}_g^0 - \mathcal{V}_d^0}{\xi_D^0} \left[\frac{1}{A^0 \xi_D^0 |\mathcal{V}_g^0 - \mathcal{V}_d^0| \Delta t + 1} - 1 \right],$$

where we have introduced

$$\text{(33)} \qquad \xi_D = \frac{1}{\rho} + \frac{1}{\beta}.$$

Once the momentum equations have been solved, we can use the form of the energy equations to calculate the corresponding changes in energy of each phase. The right-hand side of (29f) corresponds exactly to the change in kinetic energy of the dust corresponding to the change in momentum, and hence the internal energy of the dust remains constant in this step. The dust energy Ω is simply updated by the change in kinetic energy resulting from the momentum update.

The right-hand side of the gas energy equation (29c) is just the negative of the right-hand side of (29f), as required by conservation of total energy. Hence the gas energy E is updated by the negative of the update to Ω calculated above in order to leave the total energy unchanged. This energy change models both the change in kinetic energy in the gas and also a change in internal energy due to drag dissipation and the resulting heating of the gas.

Note that if the time step is large relative to the drag relaxation time, then the gas and dust velocities determined by the momentum updates (32) both approach the common equilibrium value

$$\text{(34)} \qquad \mathcal{V}_{\text{eq}} = \frac{\rho^0 \mathcal{V}_g^0 + \mathcal{V}_d^0 \beta^0}{\rho^0 + \beta^0}.$$

The source terms for heat transfer have the form

$$\text{(35a)} \qquad \frac{\partial \rho}{\partial t} = 0,$$

$$\text{(35b)} \qquad \frac{\partial}{\partial t}(\rho \mathcal{V}_g) = 0,$$

$$\text{(35c)} \qquad \frac{\partial E}{\partial t} = -\mathcal{Q}(T_g - T_d),$$

$$\text{(35d)} \qquad \frac{\partial \beta}{\partial t} = 0,$$

$$\text{(35e)} \qquad \frac{\partial}{\partial t}(\beta \mathcal{V}_d) = 0,$$

$$\text{(35f)} \qquad \frac{\partial \Omega}{\partial t} = \mathcal{Q}(T_g - T_d),$$

with initial data ρ^0, β^0, $(\rho\mathcal{V}_g)^0$, $(\rho\mathcal{V}_d)^0$, E^0, Ω^0 coming from the result of applying the drag terms, as described above. In this step the densities and momenta remain constant and only the energies change due to heat transfer between the dust and gas. It follows that the Reynolds and Nusselt numbers are constant; hence $\mathcal{Q}$ is constant and equal to its initial value $\mathcal{Q}^0$:

$$(36) \qquad \mathcal{Q}^0 = \frac{Nu^0\,6\kappa_g\beta^0}{\rho_d d^2}.$$

By using $\varepsilon_g = c_{vg}T_g$, $\varepsilon_d = c_{vd}T_d$, where c_{vg}, c_{vd} are the specific heats at constant volume, we obtain a system of two ODEs for the temperature of each phase,

$$(37\text{a}) \qquad \frac{\partial T_g}{\partial t} = -\frac{1}{\rho^0 c_{vg}}\mathcal{Q}^0(T_g - T_d),$$

$$(37\text{b}) \qquad \frac{\partial T_d}{\partial t} = \frac{1}{\beta^0 c_{vd}}\mathcal{Q}^0(T_g - T_d).$$

These can be solved and used to compute the energy updates:

$$(38\text{a}) \qquad E(\Delta t) = E^0 + \frac{T_g^0 - T_d^0}{\xi_\mathcal{Q}^0}\left[e^{-\mathcal{Q}^0\xi_\mathcal{Q}^0\Delta t} - 1\right],$$

$$(38\text{b}) \qquad \Omega(\Delta t) = \Omega^0 - \frac{T_g^0 - T_d^0}{\xi_\mathcal{Q}^0}\left[e^{-\mathcal{Q}^0\xi_\mathcal{Q}^0\Delta t} - 1\right],$$

where

$$(39) \qquad \xi_\mathcal{Q} = \frac{1}{\rho c_{vg}} + \frac{1}{\beta c_{vd}}.$$

If the time step is long compared to the relaxation time for heat transfer, the two gases reach the common equilibrium temperature

$$(40) \qquad T_{\text{eq}} = \frac{\rho^0 c_{vg}T_g^0 + \beta^0 c_{vd}T_d^0}{\rho^0 c_{vg} + \beta^0 c_{vd}}.$$

6. Source terms for gravity. With gravity, the equations (27) take the form

$$(41\text{a}) \qquad \frac{\partial\rho}{\partial t} + \nabla\cdot(\rho\mathcal{V}_g) = 0,$$

$$(41\text{b}) \qquad \frac{\partial}{\partial t}(\rho\mathcal{V}_g) + \nabla\cdot(\rho\mathcal{V}_g\otimes\mathcal{V}_g + pI) = \rho\mathfrak{g} - D(\mathcal{V}_g - \mathcal{V}_d),$$

$$(41\text{c}) \qquad \frac{\partial E}{\partial t} + \nabla\cdot((E+p)\mathcal{V}_g) = \rho\mathcal{V}_g\cdot\mathfrak{g} - D(\mathcal{V}_g - \mathcal{V}_d)\cdot\mathcal{V}_d - \mathcal{Q}(T_g - T_d),$$

$$(41\text{d}) \qquad \frac{\partial\beta}{\partial t} + \nabla\cdot(\beta\mathcal{V}_d) = 0,$$

$$(41\text{e}) \qquad \frac{\partial}{\partial t}(\beta\mathcal{V}_d) + \nabla\cdot(\beta\mathcal{V}_d\otimes\mathcal{V}_d) = \beta\mathfrak{g} + D(\mathcal{V}_g - \mathcal{V}_d),$$

$$(41\text{f}) \qquad \frac{\partial\Omega}{\partial t} + \nabla\cdot(\Omega\mathcal{V}_d) = \beta\mathcal{V}_d\cdot\mathfrak{g} + D(\mathcal{V}_g - \mathcal{V}_d)\cdot\mathcal{V}_d + \mathcal{Q}(T_g - T_d),$$

where $\mathfrak{g} = (0, 0, -g)^{\mathrm{T}}$ is the gravitational acceleration in the vertical direction. The gravity term for the dust equations is handled in the fractional step procedure along with the source terms for drag and heat transfer. Since the mass is constant over a time step in solving these ODEs, the equation for momentum is easily solved by modifying the vertical velocity by $-g\beta\Delta t$ and then adjusting the energy to reflect this change in kinetic energy.

The gravity source term for the gas could be handled in the same way. However, the gas also has pressure. In hydrostatic equilibrium (as in a stationary atmosphere) there is a pressure gradient that exactly balances the gravity source term. With a fractional step approach, the jump in pressure leads to nontrivial waves in the Riemann solution computed across each cell interface, which in turn causes a change in the cell averages during the hyperbolic step. The gravitational source term then leads to a compensating change in the cell averages that ideally would exactly cancel out the changes generated by the Riemann solution. In practice this will not happen and the numerical algorithm will not maintain a steady state. In fact the errors generated can be quite significant.

Instead we use an approach that does a much better job of maintaining hydrostatic balance and that applies the second-order correction terms and limiters in the hyperbolic solver to deviations from the steady state rather than to waves that arise artificially from the pressure gradient.

We take advantage of the f-wave formulation described in section 3 and incorporate an appropriate component of the gravity source term into the jump in flux across each interface before splitting this jump into waves. In place of (24), we split

$$(42) \qquad f_g(Q_g^{\mathrm{R}}) - f_g(Q_g^{\mathrm{L}}) - \Psi = \sum_{p=1}^{3} \mathcal{Z}^p$$

into f-waves $\mathcal{Z}^p$. In solving this Riemann problem we have left and right states given by the cell averages in the cells on the two sides of the interface, with the velocities u_g^{L} and u_g^{R} taken to be the gas velocity normal to the interface from each side. On the left side, for example, we have

$$(43) \qquad Q_g^{\mathrm{L}} = \begin{bmatrix} \rho^{\mathrm{L}} \\ \rho^{\mathrm{L}} u_g^{\mathrm{L}} \\ E^{\mathrm{L}} \end{bmatrix}, \qquad f(Q_g^{\mathrm{L}}) = \begin{bmatrix} \rho^{\mathrm{L}} u_g^{\mathrm{L}} \\ \rho^{\mathrm{L}} (u_g^{\mathrm{L}})^2 + p^{\mathrm{L}} \\ u^{\mathrm{L}} (E^{\mathrm{L}} + p^{\mathrm{L}}) \end{bmatrix}.$$

The source term for this Riemann problem that we use in (42) is then

$$(44) \qquad \Psi = \Delta z \begin{bmatrix} 0 \\ -g(\rho^{\mathrm{L}} + \rho^{\mathrm{R}})/2 \\ -g(\rho^{\mathrm{L}} u_g^{\mathrm{L}} + \rho^{\mathrm{R}} u_g^{\mathrm{R}})/2 \end{bmatrix}.$$

Here $\Delta z = z^{\mathrm{R}} - z^{\mathrm{L}}$ is the difference in the vertical coordinate of the centroids of the two cells adjacent to this interface. In the hydrostatic case $u^{\mathrm{L}} = u^{\mathrm{R}} = 0$, and we expect the jump in pressure between the cell averages to approximately equal $-\Delta z\, g(\rho^{\mathrm{L}} + \rho^{\mathrm{R}})/2$, with this cancellation occurring before the waves are generated for use in the hyperbolic solver.

This approach to incorporating the gravitational source term into the Riemann solver is related to other so-called well-balanced methods for solving conservation laws with source terms in which the source terms balance the divergence of the flux in a
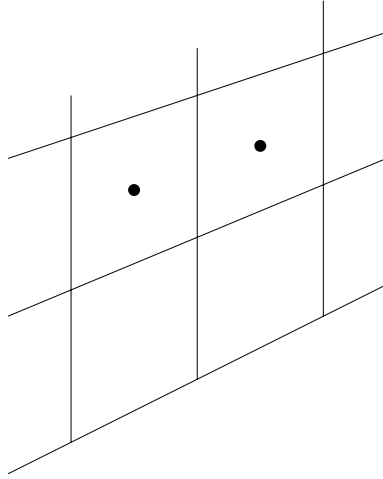
Fig. 1. *A two-dimensional mapped grid fitted to surface topography.*

nontrivial steady state. See, for example, [3, 6, 14, 15, 16, 20, 21, 28] for some other approaches. We note that the other source terms in our equations (drag, heat transfer, and the geometric source terms for axisymmetry) are nonzero only in transient regions of the flow and thus we do not need to worry about maintaining steady states and the fractional step approach we have adopted for these terms seems to work well in general. (In other applications there can exist steady states with nonzero velocities and then balancing these against the drag and heat transfer sources may be important as well.)

For applications to volcanic flows we will use a mapped grid that conforms to the ground surface, of the type shown in Figure 1 in two dimensions (blown up near the surface). A quadrilateral logically rectangular grid is used in which the horizontal grid lines are interpolated between the surface topography and a fixed upper elevation, while the vertical grid lines are still vertical. It is important to note that the gravitational source term will generally come into every Riemann solve on such a grid, even those in the x-direction that are normal to a vertical cell interface (e.g., between the two cells whose centroids are marked by dots in the figure). Since gravity does not act normal to this interface, one might be tempted to drop the source term in this normal Riemann solve. However, the difference in elevation of the cell centroids means that there will be a pressure difference in the steady state solution that must be cancelled by the source term. The expression (44) can be more formally justified by noting that the gravitational source is the gradient of the gravitational potential and hence is a covariant tensor. The directional derivative of this tensor in the coordinate direction comes into the Riemann problem across this interface, along with the normal components of the contravariant velocity.

7. Numerical experiments. We present numerical results of some test problems obtained by applying the presented dusty gas model. Second order corrections are performed in the solution of the hyperbolic portion of the system by using the monotonized centered (MC) limiter for the gas equations, and the minmod limiter for the dust equations.

In section 7.1 we consider a one-dimensional test with no gravity taken from [43].

In section 7.2 we report results of two-dimensional computations including gravity effects in the context of simulation of volcanic processes. Results on different bottom

Variable	Driver section	Driven section
p/p_{ref}	10.0	1.0
ρ/ρ_{ref}	10.0	1.0
β/ρ_{ref}	0.0001	1.0
u_g/u_{ref}	0.0	0.0
u_d/u_{ref}	0.0	0.0
T_g/T_{ref}	1.0	1.0
T_d/T_{ref}	1.0	1.0

topography and preliminary three-dimensional computations can be found in [38].

7.1. Shock tube experiment. We simulate a shock tube experiment that has been studied numerically by Saito in [43] and was originally considered in [31]. It involves high-pressure and high-density pure air ($\gamma = 1.4$) in the driver section and air laden with solid particles at room conditions in the driven section. As in [43], an extremely small amount of dust is assumed here in the driver section for numerical reasons. Dimensionless initial data are reported in Table 2. Flow variables are normalized by using as reference density ρ_{ref}, reference pressure p_{ref}, and reference temperature T_{ref} the values for air at room conditions. Moreover, the reference velocity is defined as $u_{\text{ref}} = \sqrt{\frac{p_{\text{ref}}}{\rho_{\text{ref}}}}$.

For this experiment only we adopt the constitutive relations for drag and heat transfer that are used in [43]. These slightly differ from the relations reported in section 2.1 that we normally employ. Here, instead of (9),

$$(45) \qquad C_{\mathrm{d}} = 0.46 + 28\,Re^{-0.85}.$$

Moreover, in (10) κ_g is computed as $\kappa_g = \mu c_{pg} Pr^{-1}$, where the Prandtl number is assumed to be a constant, $Pr = 0.75$, while the gas dynamic viscosity μ varies with the temperature T (see [7]):

$$(46) \qquad \mu = 1.71 \times 10^{-5} \left(\frac{T}{273}\right)^{0.77}.$$

The algorithm for the source terms described in section 5 is adapted to allow for this temperature dependent expression of μ by assuming this variable frozen at each time step in the ODE solution.

Finally, the dust particle diameter needed to compute the Reynolds number is $d = 10\,\mu$m, and the dust and gas heat coefficients at constant volume are assumed to be equal, with a dimensionless value given by $1/(\gamma - 1)$.

Following [43], we solve dimensionless equations, which are normalized by using $\ell = \frac{4\rho_d d}{3\rho_{\text{ref}}}$ as a characteristic length and $\tau = \frac{\ell}{u_{\text{ref}}}$ as a characteristic time. The computational domain is the interval $[0, 100]$, and the diaphragm is located at $x = 50$ units. We use 1000 cells (as in [43]) and CFL = 0.9.

Results of the computations at normalized time units = 5, 10, and 30 are displayed in Figures 2, 3, and 4, respectively, together with results corresponding to the case of pure gas in both the driver and driven sections for comparison.

The structure of the solution of this shock tube problem involves a left-going rarefaction wave, a contact discontinuity, and a right-going shock wave. In particular,
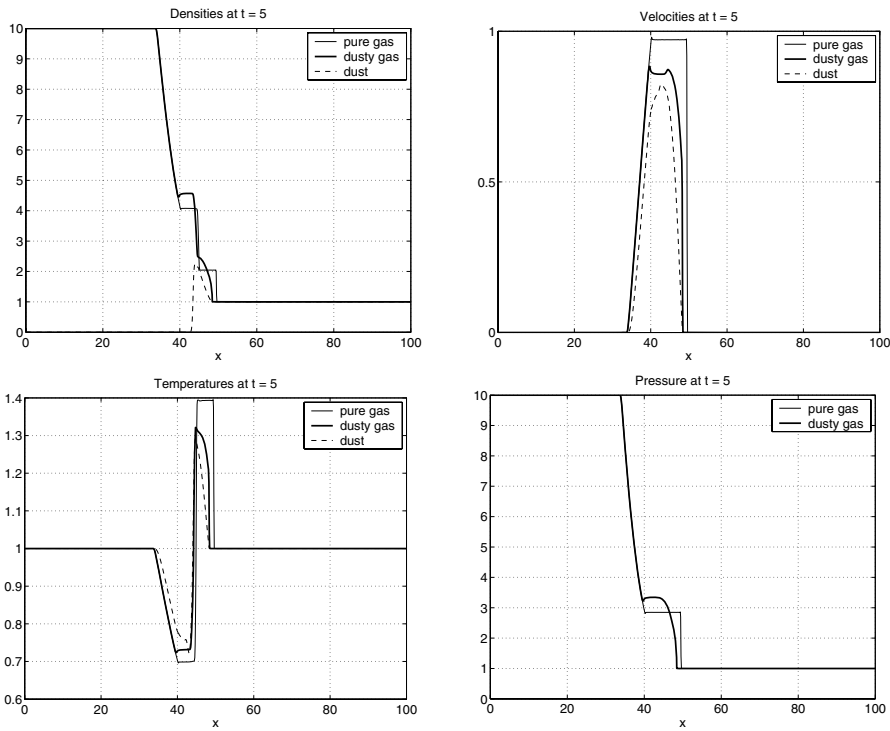
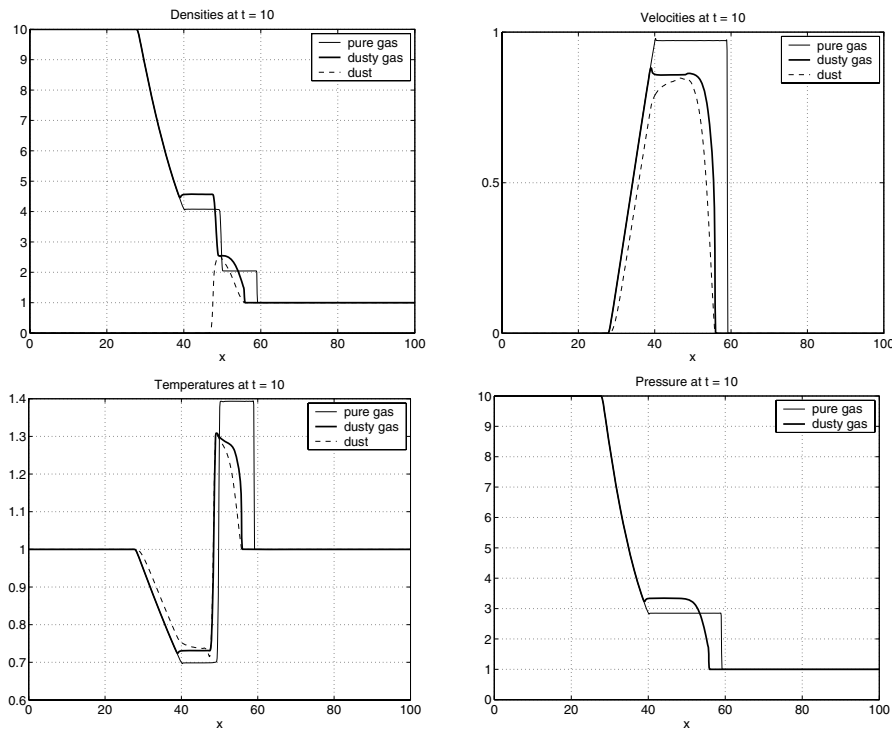FIG. 2. *Saito's experiment. Densities, velocities, temperatures, and pressure at $t = 5$.*

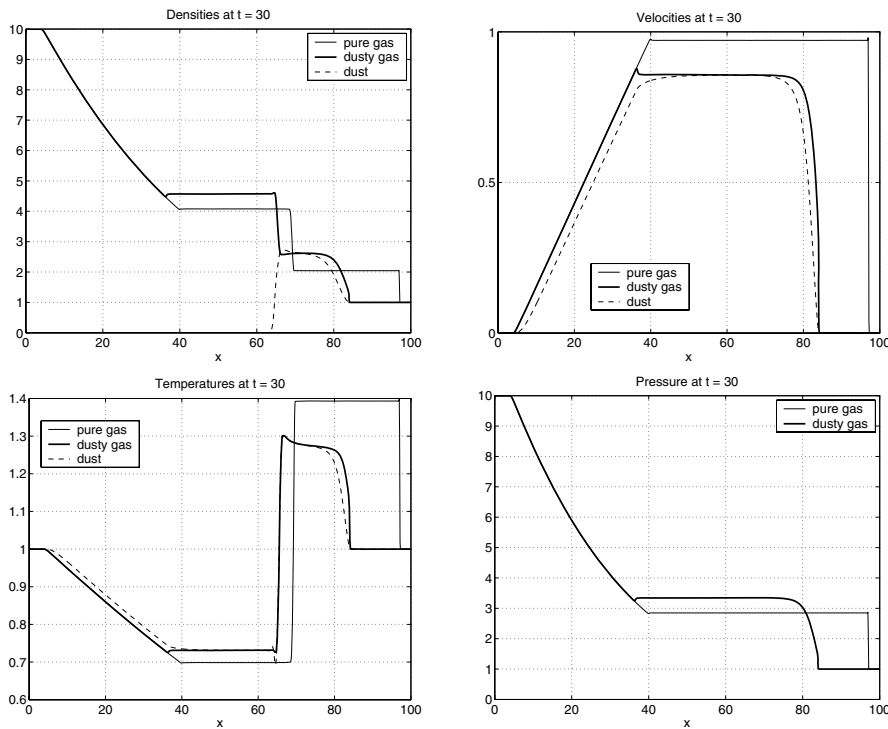FIG. 3. *Saito's experiment. Densities, velocities, temperatures, and pressure at $t = 10$.*

FIG. 4. *Saito's experiment. Densities, velocities, temperatures, and pressure at $t = 30$.*

the presence of the particulate phase leads to the development of a partially dispersed shock wave, characterized by a frozen shock in the gas followed by a relaxation region. This is formed since dust particles cannot follow any abrupt change in the gas due to their large inertia. With respect to the pure gas case, as described in [43], the dusty gas solution exhibits a deceleration of the shock front and a consequent higher compression behind it.

As time progresses, the structure of the solution tends to a stationary configuration characterized by an equilibrium region around the contact surface, and relaxation regions of constant width behind the rarefaction and shock wave. This stationary state can be observed in Figure 4, where in particular we can notice the equilibrium zones from the velocity and temperature profiles.

The results presented here agree well with those reported by Saito in [43], which are validated by the author by comparison with pseudostationary solutions obtained through numerical integration of the steady conservation equations. The numerical method of Saito is based on an operator splitting technique that uses the Harten [18] and Yee [48] scheme for the gas phase and a semianalytical approach for the dust phase. An inaccuracy in our results, not observed in [43], is the appearance of oscillations in the computed dust temperature in the neighborhood of the contact surface. These arise only when second-order corrections are performed, and they decrease with mesh refinement. We remark that oscillations are generated in the process of deriving the dust temperature from the internal energy per unit volume and dividing this by the computed dust density. No oscillations appear in the dust energy (or in other conserved variables), as shown in Figure 5. Note also that this
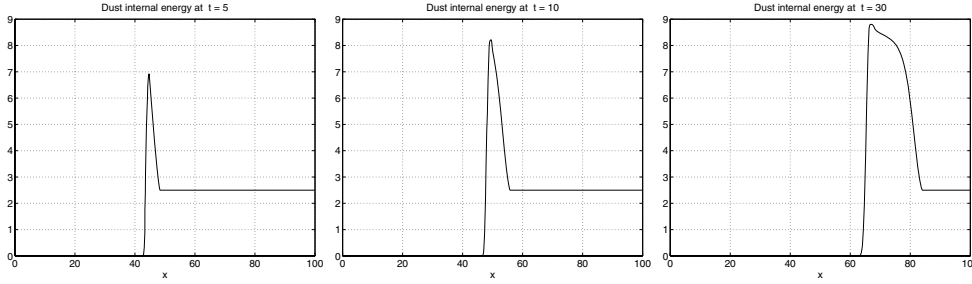
FIG. 5. *Saito's experiment. Dust internal energy per unit volume at* $t = 5, 10, 30$.

TABLE 3
Physical parameters for the two phases.

Quantity	Value	Unit
R	287.0	J/(kg K)
γ	1.4	
c_{vd}	$1.3 \cdot 10^3$	J/(kg K)
μ	$\mu = 10^{-5}$	Pa s
κ_g	0.05	W/(m K)

type of inaccuracy does not affect the computation process in our algorithm described in section 5. In fact, in the updating of the energies through (38) we actually do not need the dust temperature itself, but the product βT_d, as we can see by rewriting the term $\frac{T_g^0 - T_d^0}{\xi_Q^0}$ as $\frac{\rho c_{vg} c_{vd}}{\rho c_{vg} + \beta c_{vd}} (\beta T_g^0 - \beta T_d^0)$. This is also consistent with the form of the heat transfer source term, which can be rewritten as $\mathcal{Q}(T_g - T_d) = \mathcal{Q}'(\beta T_g - \beta T_d)$, where $\mathcal{Q}' = \frac{Nu \, 6\kappa_g}{\rho_d d^2}$. The fact that in the results of Saito this difficulty does not arise can be explained by considering that his algorithm for the dust phase uses the dust temperature as a primary variable, whereas in our case the dust temperature is derived from the conserved variables.

7.2. Explosive volcanic eruptions. We employ the dusty gas flow model presented above to simulate some of the processes that characterize explosive volcanic events. Indeed, as mentioned in the introduction, the original motivation for the development of the two-phase flow model (27) was the numerical study of volcanic phenomena. The eruption mixture in this framework is described as a two-phase flow made of gas and solid particles of a single size. In particular, the gas phase is assumed to be dry air (no water vapor content). Some of the physical parameters adopted for the two phases are reported in Table 3.

We report results of two problems from a set of simulations that we have performed with data taken from the work of Neri and Dobran [32]. The aim was to test the performance of our model in describing the dynamics of pyroclastic dispersion in the atmosphere and pyroclastic flows on the ground, and the sensitivity to the variation of some eruption parameters that influence such processes.

The physical model assumed in [32] is more complex than ours and takes into account several effects that we neglect. Among these are viscosity of the gas, turbulence, water vapor content, exchange of momentum and energy between the two phases related to the gas pressure gradient, and the dense regime for the particulate phase. Despite the simplifications of our model, we observe that we are able to capture some of the relevant features of the various eruption styles that have been described in [32], at least in the first stages of the eruption that we study here.

TABLE 4
Vent conditions for the two numerical experiments.

Simulation	D_v [m]	v_v [m/s]	$p_{g,v}$ [MPa]	T_v [K]	$\vartheta_{d,v}$	d [μm]	ρ_d [kg/m^3]
A2	100	80	0.1	1200	0.01	10	2300
A6	100	200	0.1	1200	0.01	10	2300

Additional results on the simulation of volcanic processes, including modeling of overpressured jets on different crater morphology, can be found in [38].

Initial and boundary conditions. We consider the injection of a hot supersonic particle-laden gas from a volcanic vent into a cooler atmosphere (e.g., [47, 10, 32, 33, 35, 37, 36]). Initially, a standard atmosphere vertically stratified in pressure and temperature is set all over the domain. At the vent, the gas pressure, the velocities and temperatures of the two phases, and the dust volumetric fraction are assumed to be fixed and constant.

The ground boundary is modeled as a free-slip reflector. For two-dimensional experiments, an axisymmetric configuration of the flow is used, and system (41) is rewritten in cylindrical coordinates. We obtain a new set of equations with the same form of (41) on the left-hand side, but with an additional geometric source term on the right-hand side. This additional source term is treated numerically with an operator splitting technique and by employing a Runge–Kutta solver for the corresponding system of ODEs to be solved in time. In this two-dimensional axisymmetric configuration, half of the volcanic vent, of diameter D_v, is located in the lower left-hand corner of the computational domain and the symmetry axis is modeled as a free-slip reflector, while the upper and right-hand edges of the domain are free flow boundaries and all the variables gradients are set to zero.

Vent conditions. The gas and dust phase are assumed to be in thermal and mechanical equilibrium at the vent; that is, they have the same temperature T_v and the same exit velocity v_v. Data for the two numerical tests are summarized in Table 4 (subscript v refers to the vent), together with the physical properties assumed for the dust. The nomenclature of the two simulations is borrowed from [32]. The only difference with the set of data of this work is that we do not consider the water vapor content.

Note that the data sets of these two simulations differ only in the values of the vent velocities v_v, while the other variables describing the vent conditions are the same. The results for these data presented in [32] show that the eruption column evolves with a different style depending on the exit velocity: It is collapsing for $v_v = 80$ m/s, and transitional/Plinian for $v_v = 200$ m/s. As discussed below, the same behavior is described by our simulations. In these two experiments, omitting the water vapor content does not seem to influence the column style, at least in the first minutes of the process. However, some difference can be seen; see [38] for related discussion.

Note finally that for this set of experiments the vent pressure is balanced with the atmospheric pressure at the vent exit. Vent conditions are supersonic relative to the eruptive mixture, as can be verified by using the expression of the mixture sound speed in (23), and they are representative of jet conditions after decompression in the volcanic crater [32].

7.2.1. Simulation A2: Stationary collapsing column. Figure 6 shows the evolution of the eruptive mixture as computed for simulation A2, characterized by
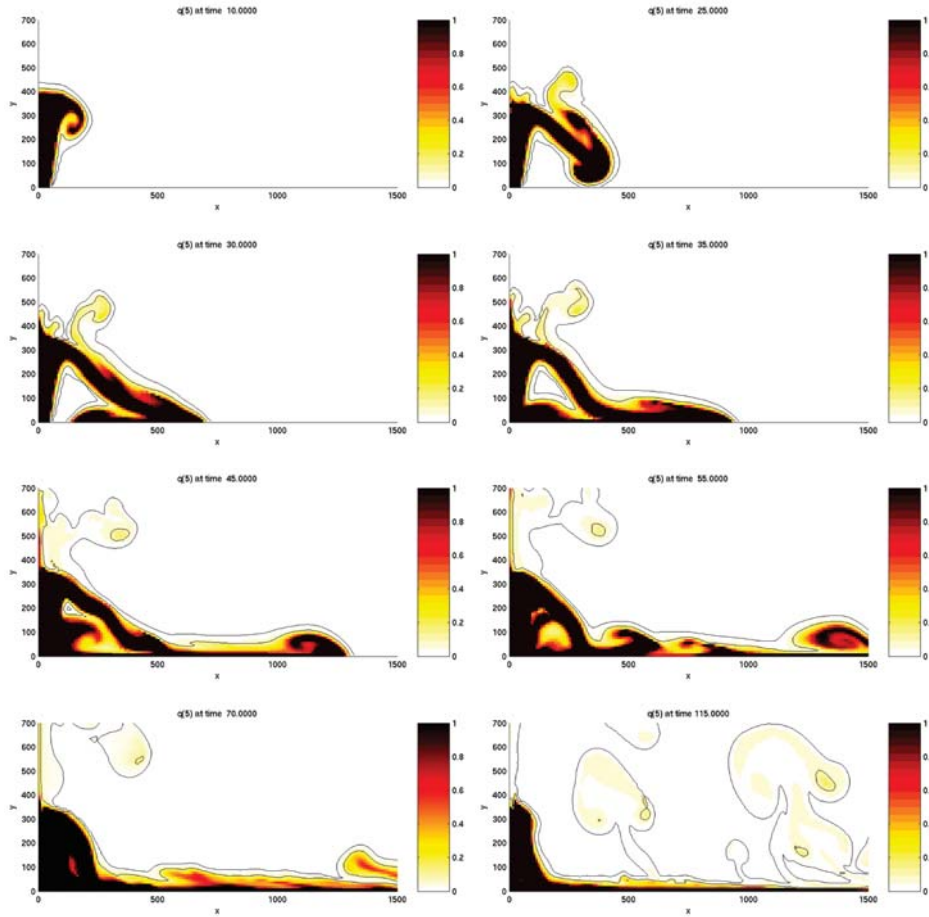
Fig. 6. *Simulation* A2. *Collapsing column. Dust density at time* $t = 10, 25, 30, 35, 45, 55, 70,$ 115 s. *Computational domain:* 3000 $m \times$ 3000 m. *Cell size* $= 10$ m (300 $\times$ 300 *cells*). *Contour values* $= 10^{[-4:1:0]}$ [kg/m^3].

$D_v = 100$ m and $v_v = 80$ m/s. In agreement with [32], we can recognize the typical features of a collapsing volcanic column, that is, fountain building above the volcanic vent, radially spreading pyroclastic flow, material recycling from the collapsed column back into the fountain, and rising of ash plumes from the pyroclastic flow. At about 10 s and 400 m above the vent the two-phase flow jet loses its vertical thrust and begins to form a collapsing column. After the collapsed column has hit the ground, material starts being recycled into the fountain. As the time evolves, the impact distance from the vent decreases and the column tends to stabilize with a steady narrow shape (as observed in [32]).

In Figure 7 we display results computed on two different grid resolutions (cell size $= 10$ m on the left and cell size $= 5$ m on the right). We can see that a smaller cell size produces a longer runout of the pyroclastic flow and a smaller thickness, but there is no notable difference in the fountain height and in the dynamics of the collapse. The significant difference in the location of the flow head on the ground can be in part related to the type of free-slip boundary condition used, though the same effect of the
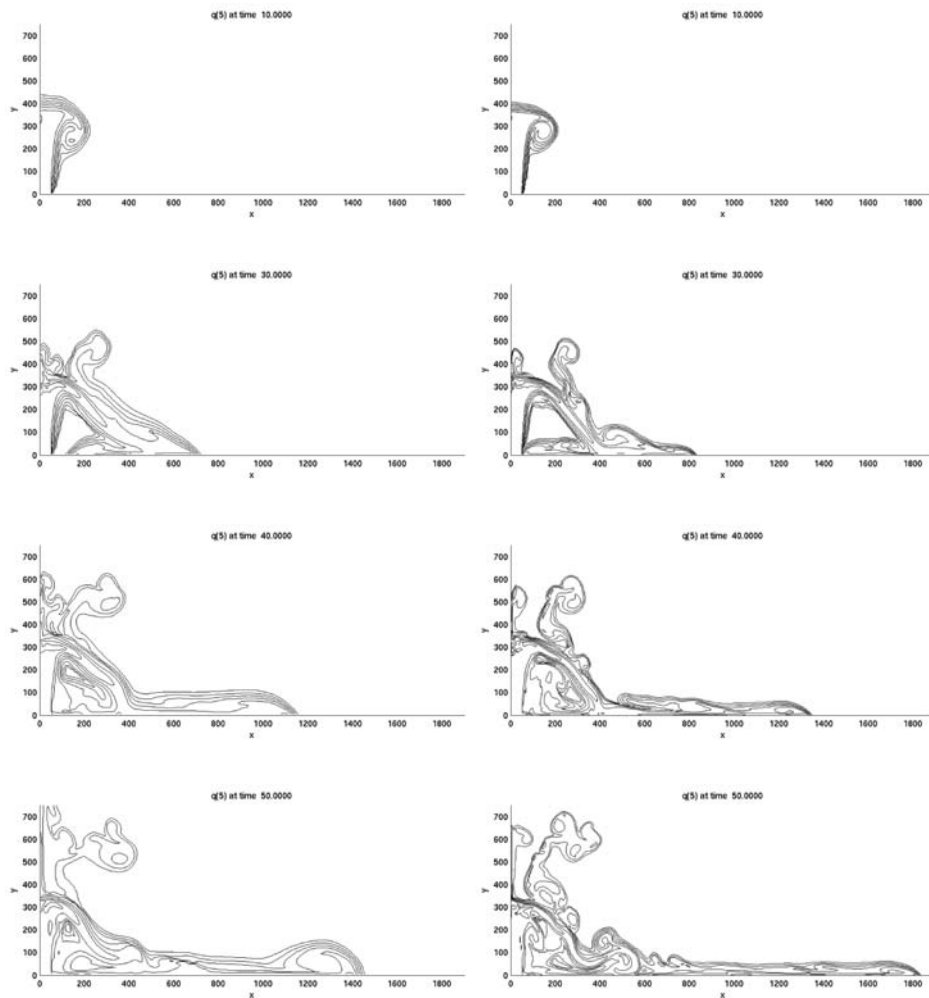
FIG. 7. *Simulation* A2. *Comparison between two different grid resolutions. Dust density at time* $t = 10, 30, 40, 50$ *s. Left:* $\Delta x = 10\,m$; *right:* $\Delta x = 5\,m$. *Contour values* $= 10^{[-5:.5:2]}$ $[\text{kg/m}^3]$.

grid resolution has also been observed in [10], where a no-slip boundary condition is employed.

In Figure 8 we highlight the features of the recirculation region displaying a contour plot of the dust density together with the gas velocity vector field, as computed on the finest grid.

Relating our results with those in [32], we see good agreement between plots of physical quantities. In particular, the column height and the column impact distance are comparable. There is a difference in the length of the runout of the pyroclastic flow, which is larger in our computations. This is not surprising, since we use a free-slip boundary condition on the ground, whereas in [32] a no-slip condition is used (consistent with the fact that their model contains viscous terms).

7.2.2. Simulation A6: Transitional/Plinian column. Figure 9 shows the results for simulation A6, which has the same vent diameter $D_v = 100\,\text{m}$ as A2, but
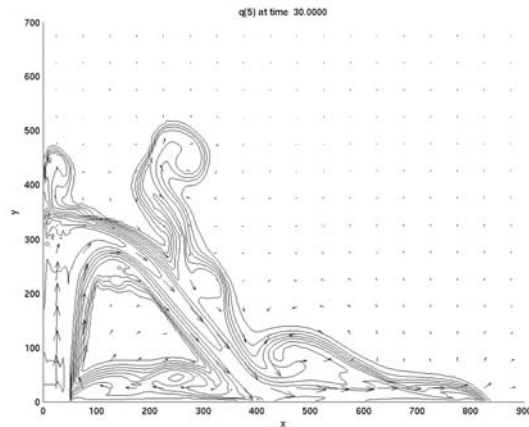
FIG. 8. *Simulation* A2. *Dust density contours and gas velocity vector field at $t = 30$ s. Contour values $= 10^{[-5:.4:2]}$ [kg/m^3]. Computational domain: 2000 m $\times$ 1000 m. Cell size $= 5$ m (400 $\times$ 200 cells).*
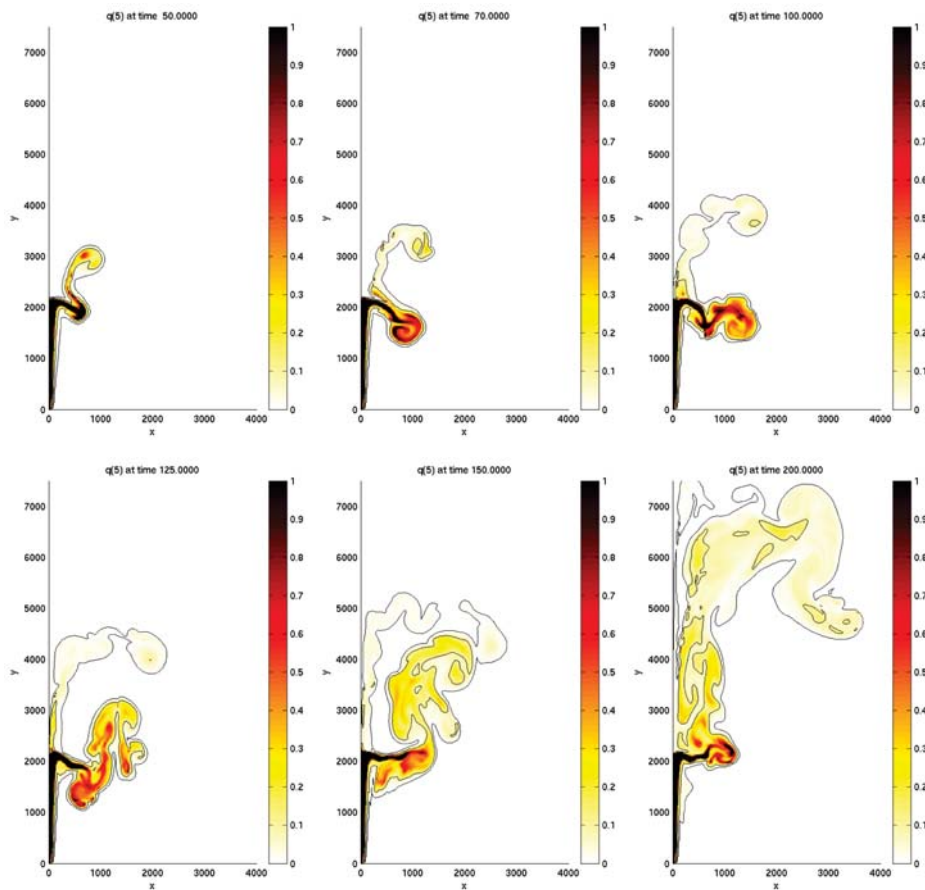

FIG. 9. *Simulation* A6. *Dust density at time $t = 50$, 70, 100, 125, 150, 170 s. Contour values $= 10^{[-5:1:0]}$ [kg/m^3]. Computational domain: 5000 m $\times$ 9000 m. Cell size $= 25$ m (200 $\times$ 360 cells).*

a greater exit velocity, $v_v = 200\,\text{m/s}$. The increase in the jet velocity (keeping D_v fixed) generates a much more buoyant column, which in this case appears of transitional/Plinian type, consistent with the observations in [32]. This column reaches a height of about 2200 m and then begins to form a radially suspended flow with some material rising buoyantly on the top, and other material attempting instead to collapse. The eruptive mixture later develops as a buoyant column. Our plots show qualitative agreement with those displayed in [32], and in particular the column height is about the same.

8. Conclusions and extensions. We have considered a model for dusty gas flow that consists of the compressible Euler equations for the gas coupled to a similar (but pressureless) system of equations for the mass, momentum, and energy of the dust. These sets of equations are coupled via drag terms (depending on the velocity difference between dust and gas) and heat transfer (depending on the temperature difference). A high-resolution wave-propagation algorithm has been used to solve the equations numerically. This finite volume method is based on solving Riemann problems at cell interfaces. The source term modeling the effect of gravity on the gas is incorporated into the Riemann solver in order to minimize numerical artifacts that could arise from splitting this source term from the pressure gradient. Other source terms (drag, heat transfer, and the gravitational force on the dust) are handled with a fractional step approach.

The one-dimensional algorithm has been shown to give agreement with results presented by Saito [43]. The two-dimensional algorithm has been applied to model explosive volcanic eruptions in which an axisymmetric jet of hot dusty gas is injected into the atmosphere. Two test cases have been presented, one in which the jet collapses into a flow along the surface, and a second, at higher velocity, where the jet rises as a Plinian column. The expected behavior is observed in each case, based on results of other researchers.

Additional test cases are presented in [38], where it is also demonstrated that adaptive mesh refinement can be successfully applied to this problem using the AMR-CLAW software in CLAWPACK [26]. Some preliminary computations in three space dimensions are also presented in [38] and compared to the two-dimensional axisymmetric results. Three-dimensional modeling over realistic topography such as Mount St. Helens is currently being investigated with an extension of this code.

Because the speed of sound in a dusty gas is much lower than in a pure gas (see section 2.2), volcanic jets can easily be supersonic and hence the jet can exhibit complex internal shock structures [22]. Some numerical study of this structure is presented in [38] and compared with some examples considered in the work of Esposti Ongaro and Neri [12]. In a joint research project with these researchers, we are continuing our study of volcanic jets using the methodology described in this paper. Further results will be presented elsewhere [13].

REFERENCES

[1] N. ANDRIANOV AND G. WARNECKE, *The Riemann problem for the Baer–Nunziato two-phase flow model*, J. Comput. Phys., 195 (2004), pp. 434–464.

[2] D. S. BALE, R. J. LEVEQUE, S. MITRAN, AND J. A. ROSSMANITH, *A wave propagation method for conservation laws and balance laws with spatially varying flux functions*, SIAM J. Sci. Comput., 24 (2002), pp. 955–978.

[3] N. BOTTA, R. KLEIN, S. LANGENBERG, AND S. LÜTZENKIRCHEN, *Well balanced finite volume methods for nearly hydrostatic flows*, J. Comput. Phys., 196 (2004), pp. 539–565.

[4] F. Bouchut and F. James, *Duality solutions for pressureless gases, monotone scalar conservation laws, and uniqueness*, Comm. Math. Phys., 24 (1999), pp. 2173–2189.

[5] D. A. Calhoun, P. Colella, and R. J. LeVeque, chombo-claw software, available online from http://www.amath.washington.edu/~calhoun/demos/ChomboClaw.

[6] P. Cargo and A.-Y. LeRoux, *Un schéma équilibre adapté au modèle d'atmosphère avec termes de gravité*, C. R. Acad. Sci. Paris Sér. I Math., 318 (1994), pp. 73–76.

[7] S. Chapman and T. G. Cowling, *The Mathematical Theory of Nonuniform Gases*, Cambridge University Press, Cambridge, UK, 1970.

[8] G. Dal Maso, P. G. LeFloch, and F. Murat, *Definition and weak stability of nonconservative products*, J. Math. Pures Appl. (9), 74 (1995), pp. 483–548.

[9] S. Dartevelle, W. I. Rose, J. Stix, K. Kelfoun, and J. W. Vallance, *Numerical modeling of geophysical granular flows: 2. Computer simulations of Plinian clouds and pyroclastic flows and surges*, Geochem. Geophys. Geosyst., 5 (2004); available online from http://www.agu.org/pubs/crossref/2004.../2003GC000637.shtml.

[10] F. Dobran, A. Neri, and G. Macedonio, *Numerical simulation of collapsing volcanic columns*, J. Geophys. Res., 98 (1993), pp. 4231–4259.

[11] D. A. Drew and S. L. Passman, *Theory of Multicomponent Fluids*, Springer-Verlag, New York, 1999.

[12] T. Esposti Ongaro and A. Neri, *Flow Patterns of Overpressured Volcanic Jets*, European Geophysical Society, XXIV General Assembly, The Hague, The Netherlands, 1999.

[13] T. Esposti Ongaro, M. Pelanti, A. Neri, and R. J. LeVeque, *Structure and dynamics of underexpanded volcanic jets: A comparative study using two numerical multiphase flow models*, in preparation.

[14] L. Gosse, *A well-balanced flux-vector splitting scheme designed for hyperbolic systems of conservation laws with source terms*, Comput. Math. Appl., 39 (2000), pp. 135–159.

[15] L. Gosse, *A well-balanced scheme using non-conservative products designed for hyperbolic systems of conservation laws with source terms*, Math. Models Methods Appl. Sci., 11 (2001), pp. 339–365.

[16] J. M. Greenberg and A. Y. Leroux, *A well-balanced scheme for the numerical processing of source terms in hyperbolic equations*, SIAM J. Numer. Anal., 33 (1996), pp. 1–16.

[17] F. H. Harlow and A. A. Amsden, *Numerical calculation of multiphase fluid flow*, J. Comput. Phys., 17 (1975), pp. 19–52.

[18] A. Harten, *High resolution schemes for hyperbolic conservation laws*, J. Comput. Phys., 49 (1983), pp. 357–393.

[19] M. Ishii, *Thermo-fluid Dynamic Theory of Two-phase Flow*, Eyrolles, Paris, 1975.

[20] S. Jin, *A steady-state capturing method for hyperbolic systems with geometrical source terms*, M2AN Math. Model Numer. Anal., 35 (2001), pp. 631–645.

[21] B. Khouider and A. J. Majda, *A high resolution balanced scheme for an idealized tropical climate model*, Theor. Comp. Fluid Dyn., to appear.

[22] S. W. Kieffer and B. Sturtevant, *Laboratory studies of volcanic jets*, J. Geophys. Res., 89 (1984), pp. 8253–8268.

[23] J. G. Knudsen and D. L. Katz, *Fluid Mechanics and Heat Transfer*, McGraw-Hill, New York, 1958.

[24] J. O. Langseth and R. J. LeVeque, *A wave-propagation method for three-dimensional hyperbolic conservation laws*, J. Comput. Phys., 165 (2000), pp. 126–166.

[25] P. G. LeFloch and A. E. Tzavaras, *Representation of weak limits and definition of nonconservative products*, SIAM J. Math. Anal., 30 (1999), pp. 1309–1342.

[26] R. J. LeVeque, clawpack software, available online from http://www.amath.washington.edu/~claw.

[27] R. J. LeVeque, *Wave propagation algorithms for multi-dimensional hyperbolic systems*, J. Comput. Phys., 131 (1997), pp. 327–353.

[28] R. J. LeVeque, *Balancing source terms and flux gradients in high-resolution Godunov methods: The quasi-steady wave-propagation algorithm*, J. Comput. Phys., 146 (1998), pp. 346–365.

[29] R. J. LeVeque, *Finite Volume Methods for Hyperbolic Problems*, Cambridge University Press, Cambridge, UK, 2002.

[30] R. J. LeVeque, *The dynamics of pressureless dust clouds and delta waves*, J. Hyperbolic Differ. Equ., 1 (2004), pp. 315–327.

[31] H. Miura and I. I. Glass, *On a dusty-gas shock tube*, Proc. R. Soc. Lond. Ser. A, 382 (1982), pp. 373–388.

[32] A. Neri and F. Dobran, *Influence of eruption parameters on the thermofluid dynamics of collapsing volcanic columns*, J. Geophys. Res., 99 (1994), pp. 11833–11857.

[33] A. NERI AND G. MACEDONIO, *Numerical simulation of collapsing volcanic columns with particles of two sizes*, J. Geophys. Res., 101 (1996), pp. 8153–8174.

[34] A. NERI, G. MACEDONIO, D. GIDASPOW, AND T. ESPOSTI ONGARO, *Multiparticle Simulation of Collapsing Volcanic Columns and Pyroclastic Flows*, VSG Report 2001-2, Volcano Simulation Group, Istituto Nazionale di Geofisica e Vulcanologia, Pisa, Italy, 2001.

[35] A. NERI, A. DI MURO, AND M. ROSI, *Mass partition during collapsing and transitional columns by using numerical simulations*, J. Volcanol. Geotherm. Res., 115 (2002), pp. 1–18.

[36] A. NERI, T. ESPOSTI ONGARO, G. MACEDONIO, AND D. GIDASPOW, *Multiparticle simulation of collapsing volcanic columns and pyroclastic flows*, J. Geophys. Res., 108 (2003), pp. 1–22.

[37] A. NERI, P. PAPALE, AND G. MACEDONIO, *The role of magma composition and water content in explosive eruptions: 2. Pyroclastic dispersion dynamics*, J. Volcanol. Geotherm. Res., 87 (1998), pp. 95–115.

[38] M. PELANTI, *Wave Propagation Algorithms for Multicomponent Compressible Flows with Applications to Volcanic Jets*, Ph.D. thesis, University of Washington, Seattle, 2005.

[39] P. L. ROE, *Approximate Riemann solvers, parameter vectors, and difference schemes*, J. Comput. Phys., 43 (1981), pp. 357–372.

[40] L. SAINSAULIEU, *An Euler system modeling vaporizing sprays*, in Dynamics of Heterogeneous Combustion and Reacting Systems (Progress Series in Aeronautics and Astronautics), Vol. 152, A. L. Kuhl, J.-C. Leger, A. A. Borisov, and W. A. Sirignano, eds., American Institute of Aeronautics and Astronautics, Washington, D.C., 1993, pp. 280–305.

[41] L. SAINSAULIEU, *Finite volume approximation of two-phase fluid flows based on an approximate Roe-type Riemann solver*, J. Comput. Phys., 121 (1995), pp. 1–28.

[42] L. SAINSAULIEU, *Traveling waves solution of convection-diffusion systems whose convection terms are weakly nonconservative: Application to the modeling of two-phase fluid flows*, SIAM J. Appl. Math., 55 (1995), pp. 1552–1576.

[43] T. SAITO, *Numerical analysis of dusty-gas flows*, J. Comput. Phys., 176 (2002), pp. 129–144.

[44] G. A. VALENTINE AND K. H. WOHLETZ, *Numerical models of Plinian eruption columns and pyroclastic flows*, J. Geophys. Res., 94 (1989), pp. 1867–1887.

[45] G. B. WALLIS, *One-Dimensional Two-Phase Flow*, McGraw-Hill, New York, 1969.

[46] K. H. WOHLETZ, T. R. MCGETCHIN, M. T. SANFORD II, AND E. M. JONES, *Hydrodynamic forming of caldera-forming eruptions: Numerical models*, J. Geophys. Res., 89 (1984), pp. 8269–8285.

[47] K. H. WOHLETZ AND G. A. VALENTINE, *Computer simulations of explosive volcanic eruption*, in Magma Transport and Storage, M. P. Ryan, ed., John Wiley, New York, 1990, pp. 113–135.

[48] H. C. YEE, *Upwind and Symmetric Shock-Capturing Schemes*, NASA Ames Technical Memorandum 89464, 1987.